



Copyright © 1997. Paper 1-005, 9,180 Words, 18 Figures.
<http://EarthInteractions.org>

Multiparameter AVHRR-Derived Products for Arctic Climate Studies

Walter N. Meier,* James A. Maslanik,* Jeffrey R. Key**
and Charles W. Fowler*

*Colorado Center for Astrodynamics Research, University of Colorado, Boulder
Colorado

**Department of Geography, Boston University, Boston Massachusetts

Received 7 October 1996; accepted 3 September 1997.

ABSTRACT: Generation and sample applications of an integrated set of remotely sensed products for investigations of Arctic climate are described. Cloud fraction, ice surface temperature, surface albedo, downwelling radiative fluxes, ice motion vectors, and cloud properties such as optical depth, phase, and droplet effective radius are estimated from calibrated and navigated AVHRR 1.1-km imagery of the Arctic Beaufort Sea region for June 1992 through July 1993. The processing strategy and characteristics of the products are reviewed. The utility of this type of multiparameter dataset for modeling applications and process studies is illustrated using simple examples of an albedo parameterization, sensible heat flux calculation, and sea ice advection.

KEYWORDS: Ice mechanics and air/sea/ice exchange; Arctic region; Remote sensing; Instruments and techniques

* Mr. Walter N. Meier, Colorado Center for Astrodynamics Research, University of Colorado, Campus Box 431, Boulder, CO 80309-0431.

E-mail address: Walter.Meier@colorado.edu

1. Introduction

The polar regions play an important role in the global climate due in part to the effects of sea ice and cloud cover on albedo and energy transfer. Turbulent heat fluxes during winter and solar energy absorbed by the ocean in summer are controlled largely by the open-water area and lead fraction in the ice pack, while radiative fluxes are regulated primarily by solar insolation, cloud properties, and surface albedo/emissivity. Efforts to gain a better understanding of these interactions require a combination of observations, modeling, and remote sensing. Since sea ice and cloud conditions can vary dramatically from day to day on spatial scales of hundreds of kilometers, datasets are needed that provide frequent temporal sampling and broad spatial coverage. Ideally, these data products should describe the distribution of the ice cover and the energy balance components that affect growth and melt of the ice pack (Barry et al., 1993). Satellite data from the National Oceanic and Atmospheric Administration (NOAA) Advanced Very High Resolution Radiometer (AVHRR) are capable of providing many of these parameters over a time span sufficient to study interannual variability. The AVHRR record, extending from the early 1980s to the present, offers complete daily coverage of the polar regions at a spatial scale well suited to sea ice and energy balance mapping and monitoring.

Using thermal-band imagery from the *Nimbus-7* Temperature and Humidity Infrared Radiometer (THIR), Comiso (Comiso, 1994) demonstrated the potential for retrieving a time series of skin temperatures over ice and snow from meteorological satellite imagery for the entire Arctic and Antarctic. AVHRR data, though, have been underutilized for polar climate studies, and only recently have algorithms and processing schemes been applied to map polar conditions. Case studies have examined algorithm performance for ice feature mapping (Burns et al., 1992; Emery et al., 1994), ice motion (Emery et al., 1995), ice temperature and albedo (Key and Haefliger, 1992; de Abreu et al., 1994; Key et al., 1997), cloud cover (Key and Barry, 1989; Key, 1996a), radiative fluxes (Key, 1996a), and turbulent fluxes (Walter et al., 1995). Fewer studies have addressed a time series of AVHRR data (Lindsay and Rothrock, 1994a; Lindsay and Rothrock, 1994b), and these studies are limited to retrievals of one or two parameters. Only the International Satellite Cloud Climatology Project (ISCCP) has attempted to produce multiyear coverages of sets of variables available for the polar regions (Rossow and Schiffer, 1991). However, the ISCCP products have a relatively low spatial resolution and until recently have not been optimized for polar applications.

The objective of this work is to introduce a new suite of AVHRR-derived products useful for monitoring and modeling the Arctic ice–climate system. These products include ice surface (skin) temperature and broadband albedo, cloud properties (fractional coverage, optical depth, phase, particle effective radius, temperature, and cloud height), downwelling radiative fluxes, and ice motion vectors. The basic approach and portions of the product set are described, and sample applications are included to illustrate possible uses of the datasets. These products represent a preliminary step in the development of similar products for the entire Arctic and Antarctic regions as part of the National Aeronautics and Space Ad-

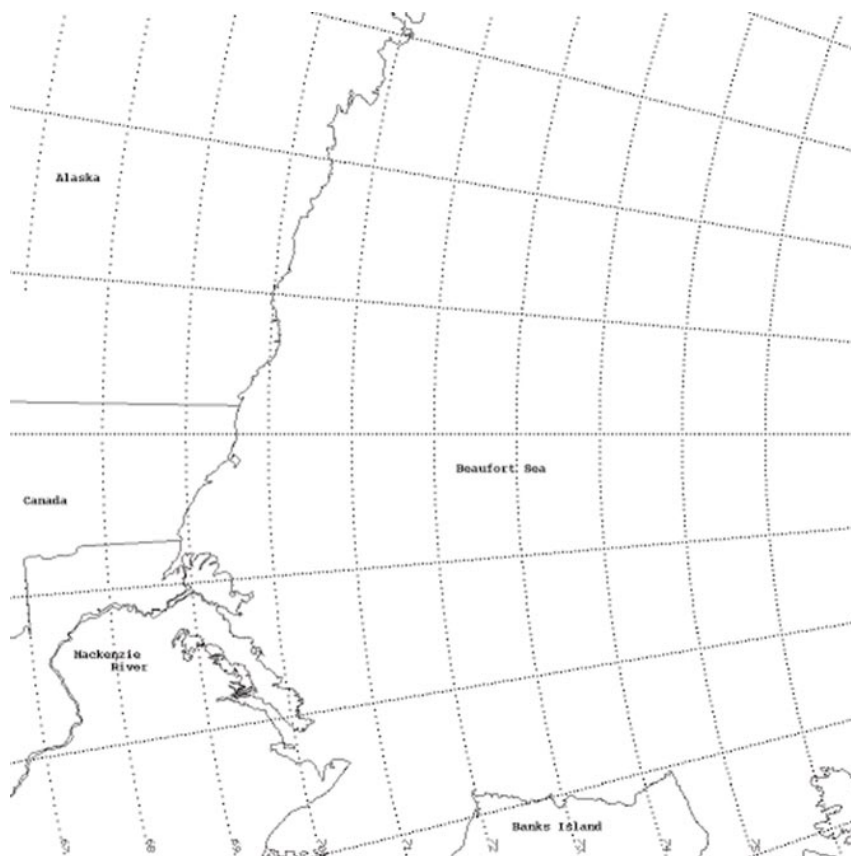


Figure 1. Map of Beaufort Sea region where AVHRR data were acquired. North is to the right in this and subsequent images.

ministration (NASA) Pathfinder effort (e.g., the AVHRR Polar Pathfinder) (Maslanik et al., 1997).

2. Study area and AVHRR preprocessing

The study area encompasses a 1.5×10^6 km² region that includes the Beaufort Sea and portions of the Canadian Arctic Basin (Figure 1). Sea ice conditions range from highly variable ice cover in the marginal ice zones at the southern edge of the study area, to perennial ice cover in the north. Cloud cover is predominantly stratus in the summer and low-level ice cloud in winter, with lower-tropospheric temperature inversions and ice crystal precipitation common in winter.

This study uses *NOAA-11* AVHRR High Resolution Picture Transmission data acquired by the Canadian Atmospheric Environment Service at their Edmonton, Alberta, receiving station. AVHRR images were collected from 12 June 1992 to 4 August 1993 with a 2-month data gap from 14 August 1992 to 11

October 1992 and other smaller gaps, yielding 293 images over a 412-day period. Since the NOAA satellites are in sun-synchronous orbits, each day's data were obtained at approximately the same time, between 1247 and 1530 local time. Of the five AVHRR channels, two are in the visible and near-infrared portions of the spectrum centered at approximately 0.6 and 0.9 μm (hereafter referred to as channel 1 and channel 2), and three are in the thermal portion at 3.7 (channel 3), 11.0 (channel 4), and 12.0 μm (channel 5). The AVHRR has a nominal field of view of 1.1 km at nadir.

The initial processing of the data included calibration and precise geolocation. Channels 1 and 2 were calibrated using coefficients developed by the NOAA–NASA AVHRR Pathfinder Calibration Working Group. Nonlinear calibrations obtained from NOAA were applied to channels 3, 4, and 5. Calibration yields albedos for the visible channels and brightness temperatures for the thermal channels. The calibrated data were georeferenced to Earth coordinates using an orbital ephemeris model with orbit and clock time corrections (Rosborough et al., 1995; Baldwin and Emery, 1995) and ground control points to yield subpixel registration accuracy. Satellite azimuth, satellite elevation, solar zenith, and solar azimuth angles were calculated from the acquisition time of each pixel as estimated by the ephemeris model. The result of this preprocessing is a suite of once-per-day 16-bit, 1024 pixel \times 1024 pixel images mapped onto a polar stereographic grid, with 1.2-km pixels, for each of the five AVHRR channels and the four angle files.

3. Product generation

The basic processing sequence to generate the product suite from the calibrated and navigated AVHRR radiances begins with cloud detection and estimation of cloud properties, followed by the estimations of clear-sky surface temperature, broadband albedo, short- and longwave fluxes, and ice motion vectors. The cloud detection routine used here employs channels 3, 4, and 5 to distinguish between clear and cloudy sky (Key, 1996a). Separate procedures are used for daylight and polar night conditions. The cloud-detection procedure examines reflectances and temperatures to automatically determine thresholds for each day. The daytime scheme defines channel 3 reflectances used as thresholds to detect clouds. For nighttime conditions, a threshold applied to the difference between channel 4 and channel 5 brightness temperatures is used to discriminate the presence of clouds. If any pixel is labeled as “dark” based on reflectance levels, the nighttime masking procedure is used for the whole image.

Optical depth, effective radius, cloud phase, and cloud-top temperature and pressure are retrieved using the Cloud and Surface Parameter Retrieval (CASPR) software toolkit for AVHRR analysis (Key, 1996b). CASPR combines a variety of parameterizations, model-derived lookup tables, and radiative transfer code to determine cloud properties and radiative fluxes (Key, 1996a). Optical depth for water clouds is estimated based on data from Hu and Stamnes (Hu and Stamnes, 1993). Shortwave ice cloud parameterizations are taken from Ebert and Curry (Ebert and Curry, 1992). Cloud particle phase is determined from a channel 4 brightness temperature threshold. Cloud-top temperature is calculated from chan-

nel 4 brightness temperatures, the uncorrected clear-sky brightness temperature, and the visible-cloud optical depth.

The surface temperature algorithm is a function of channel 4 and 5 brightness temperatures and scan angle and is based on simulations using the LOWTRAN radiative transfer model and Arctic radiosonde data and is similar to the procedure described by Key and Haefliger (Key and Haefliger, 1992) and Key et al. (Key et al., 1997). The algorithm is accurate for clear-sky conditions only and provides surface skin temperatures.

Top-of-the-atmosphere (TOA) AVHRR radiances are converted to surface albedo through several steps. Calibrated channel 1 and channel 2 TOA values are corrected for sun–satellite–surface geometry dependence (Taylor and Stowe, 1984). Then, narrowband surface albedo is retrieved by correcting the TOA albedo for atmospheric attenuation (Koepke, 1989) and bidirectional reflectance. Finally, the narrowband values are converted to broadband albedo for clear- and cloudy-sky conditions individually using both empirical and modeled relationships (Key, 1996b). After all estimates of the surface and cloud properties have been obtained, radiative fluxes are calculated using the “Streamer” radiative transfer model (Key, 1996a).

To determine ice velocities, two-dimensional cross correlations are used to match feature locations between pairs of coregistered images typically separated by 1–3 days (Emery et al., 1991). This method has been applied successfully to many different applications, such as image registration, cloud tracking, and determining velocity vectors from AVHRR and synthetic aperture radar (SAR) data (Ninnis et al., 1986; Kwok et al., 1990). Vectors are filtered based on the local cross-correlation coefficient and correlation of individual vectors with neighboring vectors. The ice velocity is calculated by dividing the ice displacement in a pair of images by the time between the images. Visible channels are used when solar illumination is sufficient; during the polar night, thermal channels are used. Although optically thick clouds preclude mapping of ice motions, Arctic clouds are often optically thin enough to permit detection of surface features. In such cases, motions can often be tracked even though some cloud is present.

Although not discussed here, additional surface characteristics that can be derived from the AVHRR albedo and temperature images include ice fractional coverage, lead fraction and orientation (e.g. Key et al., 1993), weather fronts, and sea surface temperature in the ice-free areas.

4. Product validation and comparison

4.1. Validation with field measurements

Validation of the Beaufort AVHRR time series is hampered by a lack of continuous and spatially distributed observations. Thus, the accuracy assessment for these data is currently based on previous case studies validating the individual algorithms. (e.g., de Abreu et al., 1994; Key et al., 1994a; Key et al., 1994b; Key et al., 1996; Key et al., 1997), combined with comparisons to climatological data to provide an overview of the likely range expected for the products. A comprehensive validation of the subsequent AVHRR Polar Pathfinder products is planned

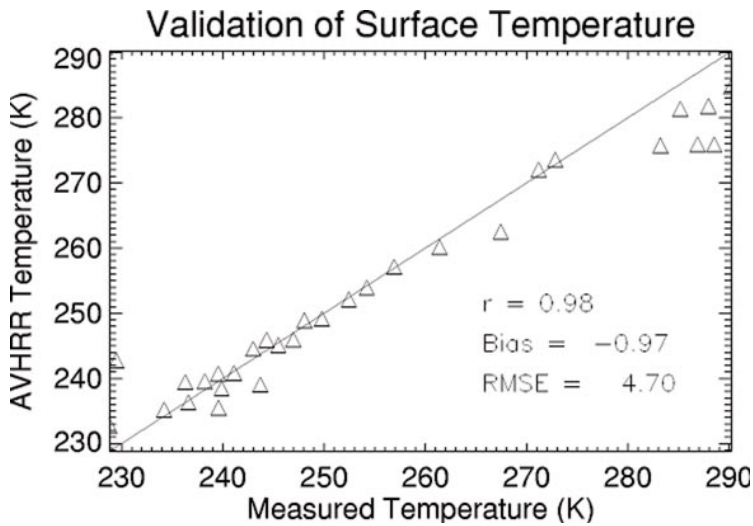


Figure 2. Comparison of satellite-derived and surface measurements of the surface (skin) temperature at Barrow, Alaska, during 1992 and 1993.

in conjunction with the Surface Heat and Energy Balance (SHEBA) field experiment in 1998.

Individual comparisons to field data suggest that the AVHRR-derived temperatures are typically within 1° – 3°C of those observed in the field (Key et al., 1994a), with the comparisons quite sensitive to field instrumentation and sampling strategy. The most thorough validation to date compared the AVHRR-derived surface temperature, broadband albedo, and downwelling flux products to field measurements made near Barrow, Alaska. These Barrow surface data were collected at NOAA's Climate Monitoring and Diagnostic Laboratory (CMDL) baseline observatory (71.32°N , 156.61°W). Although this site is situated on the Arctic tundra where complete melting of the snow occurs each summer, the site is generally considered representative of an Arctic maritime climate because the prevailing winds are northeasterly off the Beaufort Sea. All observations were made within 2 km of the coast. The region is very cloudy with high relative humidity. Surface albedo varies from 0.18 during summer to over 0.86 when snow covered. Data collected at 3-min intervals were carefully edited, calibrated, and averaged into hourly values (Stone et al., 1996). Shortwave irradiance measurements from the surface station are accurate to within 3%, on average, with systematically greater uncertainties as the signal diminishes with increasing zenith angle; the longwave values have been shown to be accurate to within about 1% (Dutton, 1993). Surface (skin) temperature and albedo are computed from the longwave and shortwave fluxes.

Comparison of the AVHRR-derived quantities with the surface observations for the pixel covering the point observations at the Barrow site are shown in Figure 2–Figure 5. Clear-sky temperature and albedo are given in Figure 2 and Figure 3, respectively. Figure 4 and Figure 5 gives the retrieved and observed

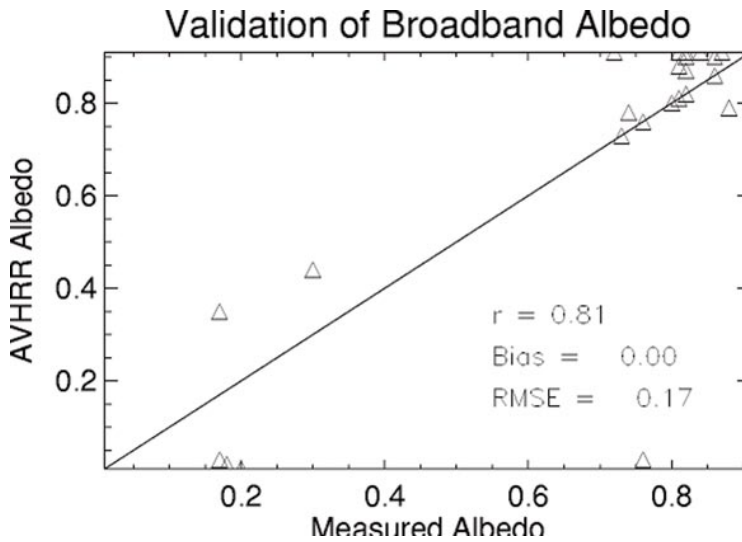


Figure 3. Comparison of satellite-derived and surface measurements of the surface broadband albedo at Barrow, Alaska, during 1992 and 1993.

downwelling shortwave and longwave flux over the annual cycle. The AVHRR-derived surface temperature estimates are quite accurate, with the exception of temperatures retrieved for summer snow-free land. This discrepancy during the summer is due to the presence of ponds and possibly ocean in the field of view, as discussed in Key et al. (Key et al., 1997). The surface albedo results are less

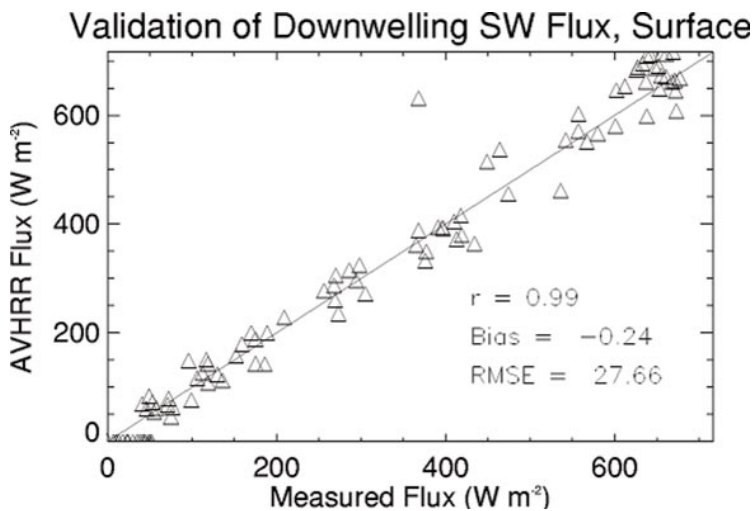


Figure 4. Comparison of satellite-derived and surface measurements of the downwelling shortwave flux at Barrow, Alaska, during 1992 and 1993.

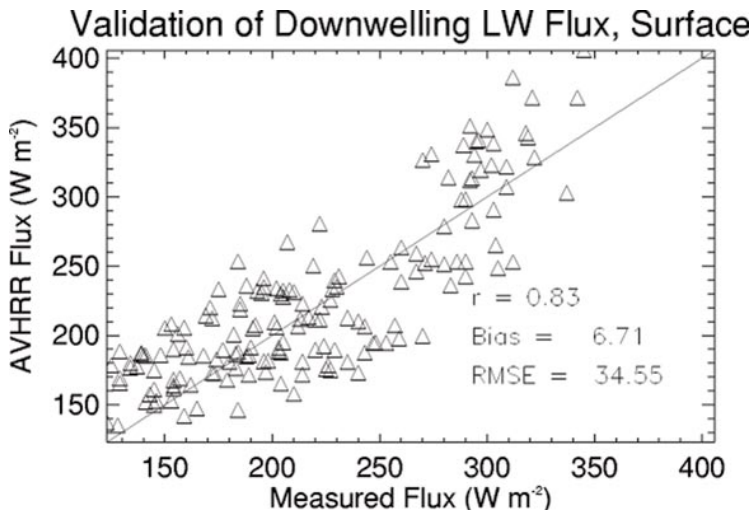


Figure 5. Comparison of satellite-derived and surface measurements of the downwelling longwave flux at Barrow, Alaska, during 1992 and 1993.

consistent, with a low bias but large rms error. Probable causes for this include residual errors in the cloud screening, and changes in aerosol amount and snow characteristics, which in turn affect the anisotropic reflectance correction and, for the latter, the narrow- to broadband conversion. However, in spite of the large variability in the broadband albedo results, the downwelling shortwave fluxes agree very well with the surface measurements.

Observations designed to address such spatial inhomogeneity over sea ice are rare. Comparisons were made to field observations collected on fast ice near Resolute Bay, Northwest Territories, which included multiyear ice, ridged ice, sastrugi, and rubble zones. Broadband albedo estimates compared to these field observations when measurements were taken coincident with satellite overpasses and for transects and grids comparable to the AVHRR field of view agree to within 4% (absolute) or 1% when restricted to highest solar zenith angles (de Abreu et al., 1994). The available comparison data were limited to only a few cases due to cloud cover, but the level of agreement provides some level of confidence for the calibration strategy and albedo algorithm.

The downwelling longwave flux estimates exhibit a small bias but a large rms error when compared to the Barrow data, with the most probable cause being errors in the cloud-base height that is estimated from the cloud-top height, the optical depth, and an assumed cloud water content. The overall time series of fluxes derived from AVHRR and averaged over the Beaufort study area are shown in Figure 6 [the high downwelling shortwave values in summer (Figure 6b) are due to the fact that the measurements are taken near midday and are not a daily average]. These results suggest that the products are likely to be most accurate for the interior of the ice pack where surface conditions are relatively uniform. When surface conditions include open water, meltponds, or leads, then the

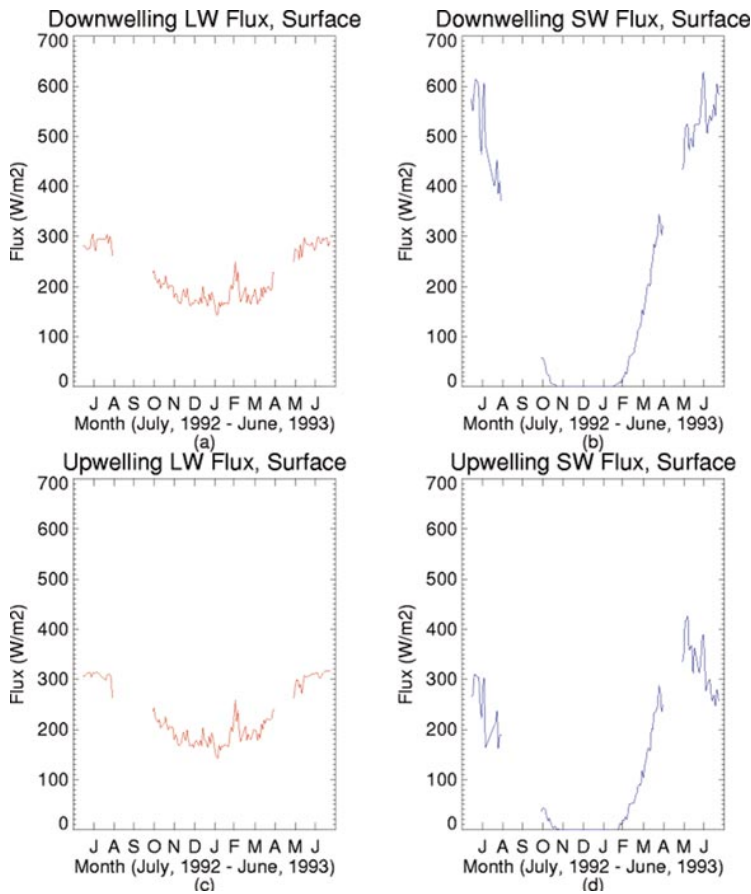


Figure 6. Time series of radiative fluxes at the surface: (a) downwelling longwave, (b) downwelling shortwave, (c) upwelling longwave, and (d) upwelling (reflected) shortwave.

AVHRR-derived albedos and temperatures over sea ice should be considered as “ice pack” values, as opposed to representing pure-pixel retrievals for ice or snow. Direct comparisons to point observations under these conditions thus will require validation datasets that provide areal coverages of different surface types as well as the albedos of these individual surfaces within the AVHRR field of view.

4.2. Comparison with climatology and other datasets

In lieu of additional long-term and/or spatially distributed field observations, another useful way of assessing the representativeness of the spatial and temporal patterns in the AVHRR-derived surface temperature, albedo, and cloud fraction products is through comparisons with gridded datasets and climatologies. The observations and one-dimensional model simulations summarized by Ebert and Curry (Ebert and Curry, 1993) and Curry and Ebert (Curry and Ebert, 1992)

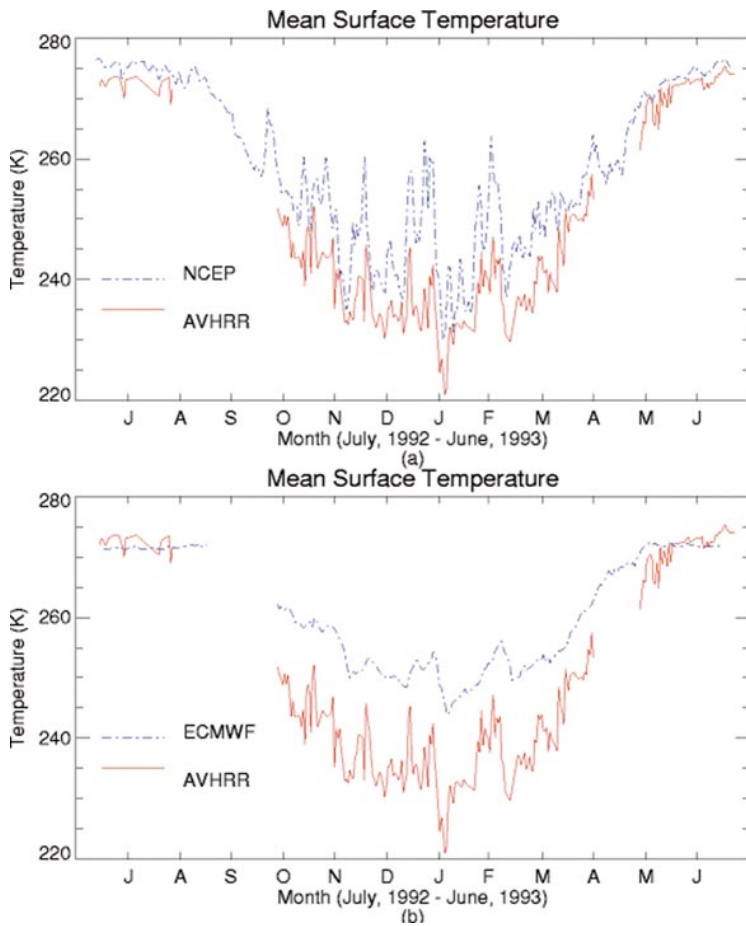


Figure 7. Time series of AVHRR-derived clear-sky surface temperature. The AVHRR temperatures are compared with surface air temperature fields from (a) NCEP reanalysis fields, (b) ECMWF fields, and (c) POLES gridded fields interpolated from surface stations.

(referred to jointly hereafter as EC) provide a useful baseline for comparison with the AVHRR-derived parameters. The information cited by EC is a collection of representative values for the Arctic derived from numerous field observations as well as physically based parameterizations and model simulations. Specifically, Curry and Ebert (Curry and Ebert, 1992) combine observations and climatologies of cloud properties and atmospheric profiles with a radiative transfer model and a one-dimensional thermodynamic ice model to generate a suite of cloud optical properties, surface albedo, and surface temperature. This internally consistent set of products thus provides a useful comparison dataset for the similar products derived here from AVHRR data. Comparisons are discussed below in terms of time series of daily means summed over the ocean area in the model domain.

The AVHRR clear-sky surface temperatures vary from 225 K to near 250 K for a given day during winter (Figure 7). Monthly average surface temperatures

range from 233 K for January to 273 K during the summer. These are within the expected ranges of values for this region and compare well with the observations and simulations given by EC (Table 1). Winter temperatures from AVHRR are lower than for the climatology, at least in part because AVHRR can obtain surface temperatures in clear-sky conditions only. Due to enhanced downwelling long-wave radiation, clouds generally warm the surface in the Arctic; thus, one would expect skin temperatures to be lower than 2-m air temperatures (Lindsay and Rothrock, 1994a).

These temperatures also compare well with other datasets (Banks and Par-tanen, 1959) (Table 1), and other analyses of AVHRR-derived ice temperatures (e.g., Lindsay and Rothrock, 1994a), even though there are differences due to the variable climate in different years of data. The Lindsay and Rothrock temperatures were derived from 1989 AVHRR images using a very similar algorithm to the one discussed in section 3. Lindsay and Rothrock, citing other results (Y. Yu, personal communication) that compare AVHRR-derived temperatures to ice stations and drifting buoys, estimate rms differences on the order of 3 K, similar to the comparison of our data with the Barrow field station (rms error, 4.7 K; Figure 2). However, Yu's results as cited by Lindsay and Rothrock were biased an average of 1.2 K higher than field data, while our values are 0.97 K lower on average. Comiso (Comiso, 1994) discusses sea ice skin temperatures retrieved from *Nimbus-7* THIR thermal-band imagery and estimates an rms error of 2 K. Depending on the observations used, though, the remotely sensed data tend to be biased higher or lower than the observations. Discrepancies among the different datasets discussed here may reflect differences in atmospheric conditions in the years analyzed, the possible presence of subresolution leads, accuracy of the cloud-detection steps, and algorithm assumptions, as well as differences in the types of in situ data used.

In another comparison, the AVHRR-derived skin temperatures correspond reasonably closely to surface air temperatures provided by meteorological forecast models [National Centers for Environmental Prediction (NCEP) reanalyses (Kal-nay et al., 1996) (Table 1 and Figure 7a); European Centre for Medium-Range Weather Forecasts (ECMWF) (Figure 7b)], and interpolated air temperatures based on surface station and drifting buoy data from the Polar Exchange at the Sea Surface (POLES) project (Figure 7c). The NCEP and ECMWF temperatures over the ice pack are essentially entirely model derived, while the POLES data are interpolated observations considered representative of 2-m air temperatures. The skin temperatures tend to be lower than the surface air temperatures in winter, consistent with the typical surface temperature inversion over sea ice, and the fact that the NCEP, POLES, and ECMWF temperatures are for cloudy and clear conditions while the AVHRR-derived temperatures are for clear sky only, as noted above. The trends in each set are similar, though there is closer agreement among NCEP, POLES, and AVHRR temperatures than between ECMWF and AVHRR. When composited over a number of days, such as for the mean April skin temperatures shown in Figure 8, the basic temperature patterns agree well with NCEP mean surface air temperatures for the same period (not shown) although the NCEP air temperatures are typically about 2 K higher than the AVHRR temperatures.

Given the low spatial resolution of the comparison datasets, these data pro-

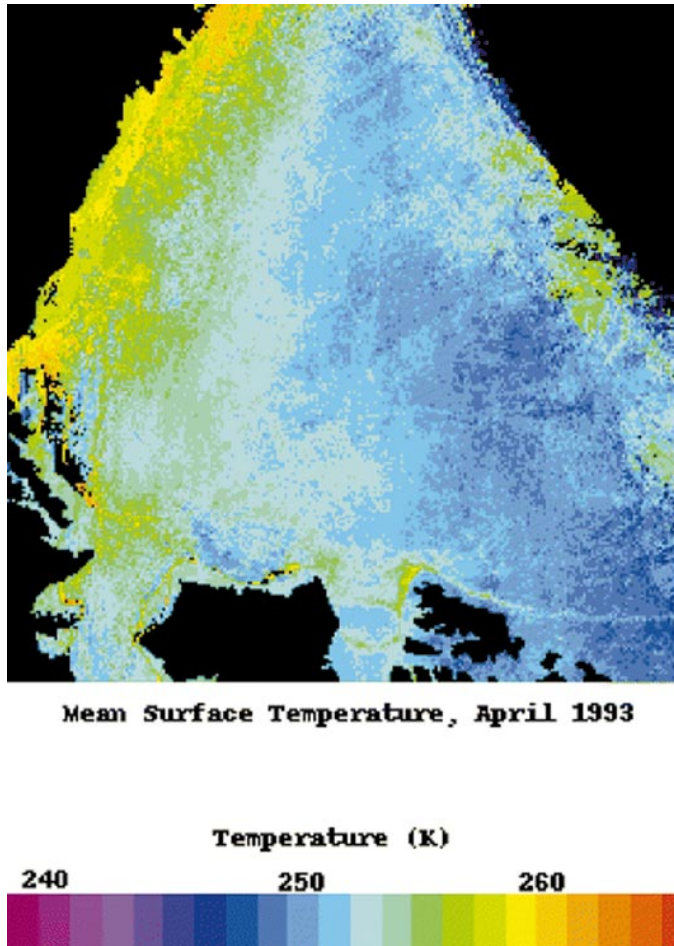


Figure 8. Mean skin temperature for April 1993 as determined from a composite of AVHRR-derived daily skin temperatures.

vide no 100% clear-sky observations that could help in assessing possible biases due to the restriction of AVHRR retrievals to clear-sky conditions. One-dimensional radiative transfer modeling such as that used by EC could be employed to simulate clear-sky-only temperatures, but such calculations have not yet been performed. In addition to field instrument error and the possible temperature bias due to clear-sky conditions, other possible sources for the apparent negative bias in the AVHRR skin temperature estimates include undetected thin, high (e.g., cold) cloud. Also, a snow emissivity is assumed that applies uniformly to all surfaces within the field of view. The presence of different surface types as well as deviation of the true snow emissivity from that used will contribute to errors. Possible routes being investigated for further reducing these errors include additional cloud-clearing steps and comparisons of prescribed surface emissivities to field measurements planned as part of the SHEBA experiment.

Albedo is also reasonably consistent with previous results (Table 2). The

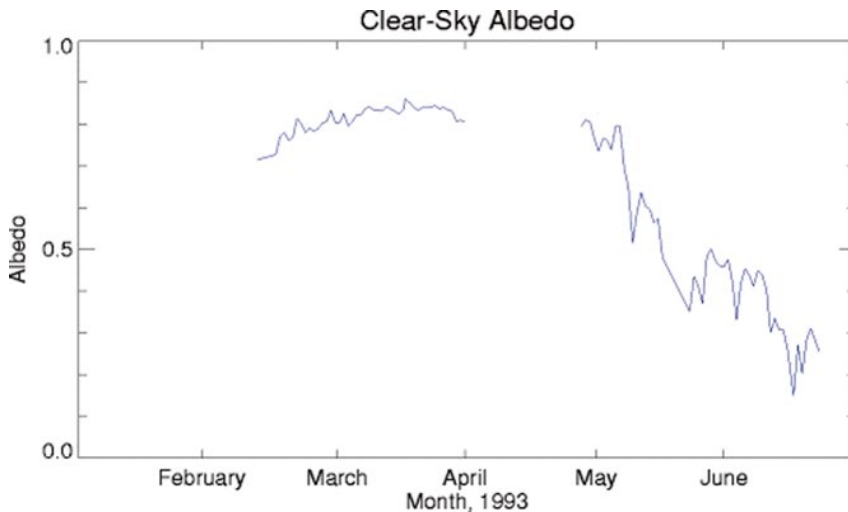


Figure 9. AVHRR-derived clear-sky broadband albedo.

monthly average albedo exhibits a maximum of 0.75 in April and then drops sharply to 0.45 by the summer (Table 2). This characteristic drop in albedo, a result of melt, occurs earlier in our data than in the EC climatology (Table 2 and Figure 9). Part of this difference is due to the marginal ice zone character of the study region. The albedo values are averaged over the whole nonland region and thus include areas of open water that develop within the ice pack and along the coast typically in late May and June. As noted in the applications example in section 5, albedo for high-concentration ice cover is 0.85 prior to melt.

Our albedo results are similar to other AVHRR-derived albedos such as those from Robinson et al. (Robinson et al., 1992) and Lindsay and Rothrock (Lindsay and Rothrock, 1994b) given in Table 2, although our values are lower in spring and early summer. Some of this difference with the EC albedos could be due to the fact that clear-sky albedos (the satellite-derived values in Table 2) tend to be lower than all-sky albedos (the EC values in Table 2) due to absorption of near-infrared radiation by clouds. Lindsay and Rothrock use manually cloud-masked images to calculate relative albedos (with albedo of pack ice in March and April set to 0.80). They estimate uncertainties in their measurements at 0.25 due to aerosols, ozone, and water vapor. This compares to uncertainties in our albedos of 0.17, as estimated from the Barrow field data (Figure 3). Also, as described above, the inclusion of some open-water areas within our estimates likely accounts for a portion of the lower albedo values. The EC albedos represent central Arctic conditions with minimal open water, while the Robinson et al. estimates exclude identifiable open-water values from the estimated ice-pack albedo. Comparisons are also complicated by the fact that the Robinson et al. albedo was estimated using prescribed albedos for ice and water (e.g., digital numbers were assigned to albedos based on a linear fit between the prescribed albedos for ice and open water). In turn, the AVHRR calibrations used here (as provided by the

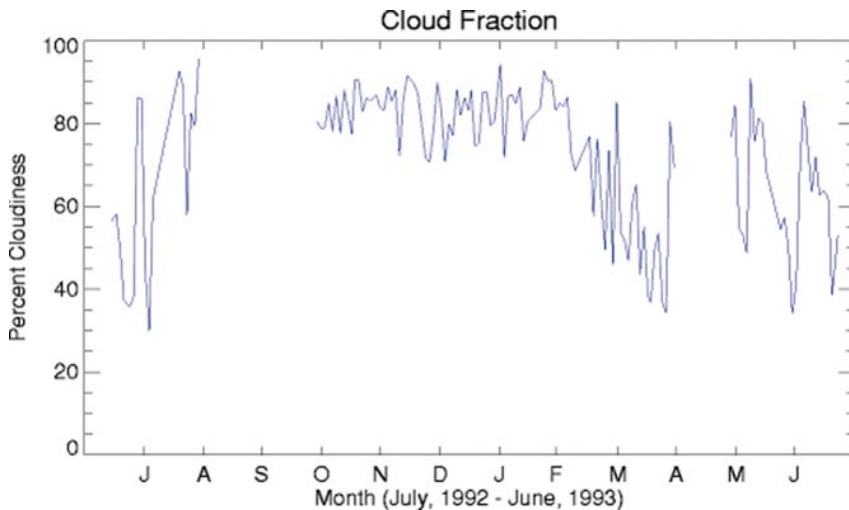


Figure 10. Time series of cloud fraction over the Beaufort Sea.

NOAA–NASA AVHRR Land Pathfinder project) may not be as accurate as desired for snow and ice. Thus, in addition to the possible sources of differences already cited, some of the differences between the remotely sensed albedos in Table 2 are likely due to choice of calibration.

The relatively high resolution of the AVHRR data provides considerable information on cloud distribution, morphology, and cloud type. Cloud fraction within the study area tends to be highly variable in late spring and summer, with values ranging from below 40% to near 90% across the region on any given day (Figure 10). Winter cloud cover is more consistent, with values generally between 70% and 90%. Monthly mean cloud fraction varies from 45% in April to near 80% in late summer and fall (Table 1). The AVHRR-derived cloud fractions lie between the climatology and ISCCP fractions, which are an average of cloud fractions for the period 1984–91. The monthly mean NCEP reanalysis cloud fractions are also significantly lower than the AVHRR products and the climatologies (Table 1). Relative to observations and consistent with other comparisons (e.g., Schweiger and Key, 1992), both satellite-derived datasets tend to underestimate cloud amount in spring and summer but the difference is less pronounced in the AVHRR products described here. These data also yield higher amounts of winter cloud fractions, which may reflect a greater sensitivity to low-level ice crystal clouds (“diamond dust”), which can be a significant portion of the cloud cover during winter but which is typically excluded from observational estimates of cloud amount (Curry and Ebert, 1992). As opposed to previous ISCCP processing, the cloud-detection algorithms employed here are specifically tuned for the Arctic, with the cloud-detection routines applied to data at higher spatial resolution. The greater cloud fractions may therefore be due to this tuning of the cloud-detection algorithms for Arctic conditions, as well as to improved detection of patchy clouds or to thin clouds that make up much of the cloudiness over the ice

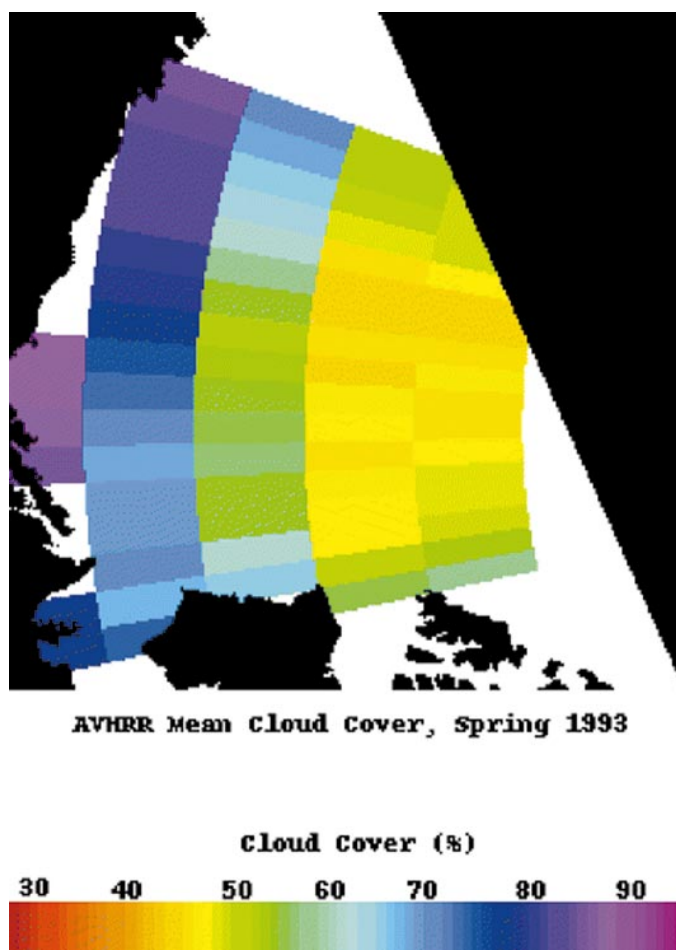


Figure 11. AVHRR-derived mean cloud fraction for March–May 1993. The AVHRR data have been regrided to correspond to the grid cell size of the NCEP model shown in Figure 12.

pack (Kukla and Robinson, 1988; Serreze and Rehder, 1990). We note that the ISCCP data used here are the ISCCP C2 product. The new D series of ISCCP data will include improved algorithms for the polar regions. In any event, given the potential for a large spatial and interannual variability in cloud amount in this region (Kukla and Robinson, 1988), these comparisons to climatologies must be considered only in general terms. As more data are processed as part of the AVHRR Polar Pathfinder, additional validations with concurrent field observations and with the ISCCP D2 data are planned.

Figure 11 and Figure 12 compare the spatial distributions of mean AVHRR-derived and NCEP-simulated cloud fractions for March–May 1993. The AVHRR data show a pronounced regional variation in cloud fraction, with much greater cloud amount over the marginal ice zones and open-water areas in the Beaufort Sea, and with reduced cloud amounts over the central Arctic. Such a pattern is

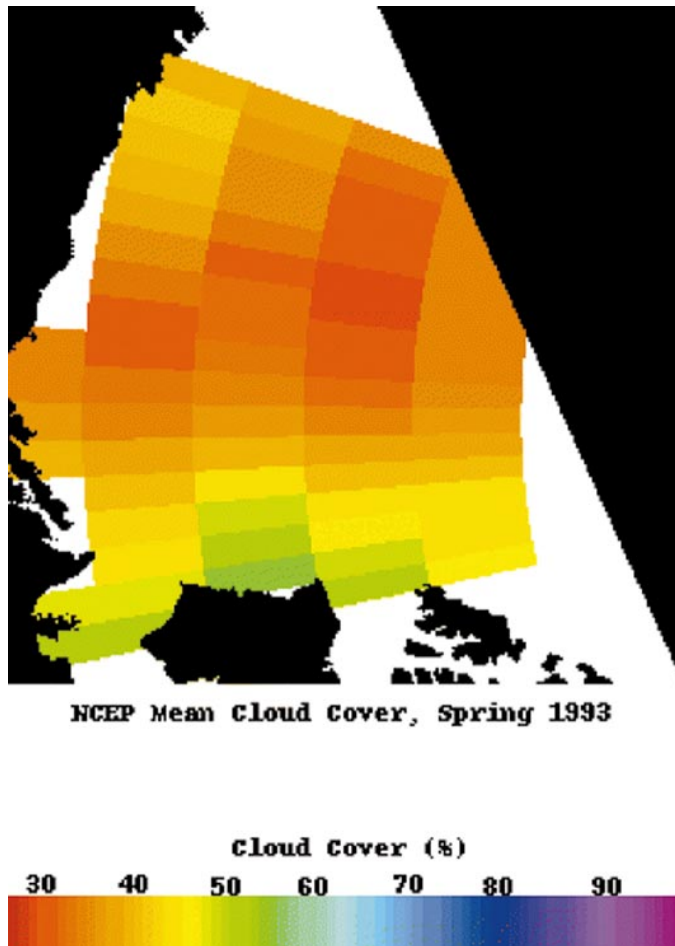


Figure 12. NCEP-derived mean cloud fraction for March–May 1993.

reasonable given the potential for cloud formation where open water is present. The underestimate of cloud amount by the NCEP model in these regions could reflect model shortcomings related to moisture advection and low-level cloud formation processes. In addition, the pattern of extensive cloudiness near the coast and clearer skies over the central ice pack in the AVHRR data suggests that climatologies that rely heavily on the interpolation of coastal observations might potentially bias the climatologies toward higher cloud amounts over the central Arctic. Schweiger and Key (Schweiger and Key, 1992) discuss such problems in more detail. Alternatively, the AVHRR cloud algorithm might simply be more effective at detecting cloud over open water and marginal ice zones, or the cloud patterns might be due to unusual conditions in 1993. As noted above, the availability of more such data for other years and areas, in combination with continuing validation efforts, should help resolve these uncertainties.

No field observations are available that provide spatial distributions of cloud properties over the Beaufort Sea during the study period. However, the derived

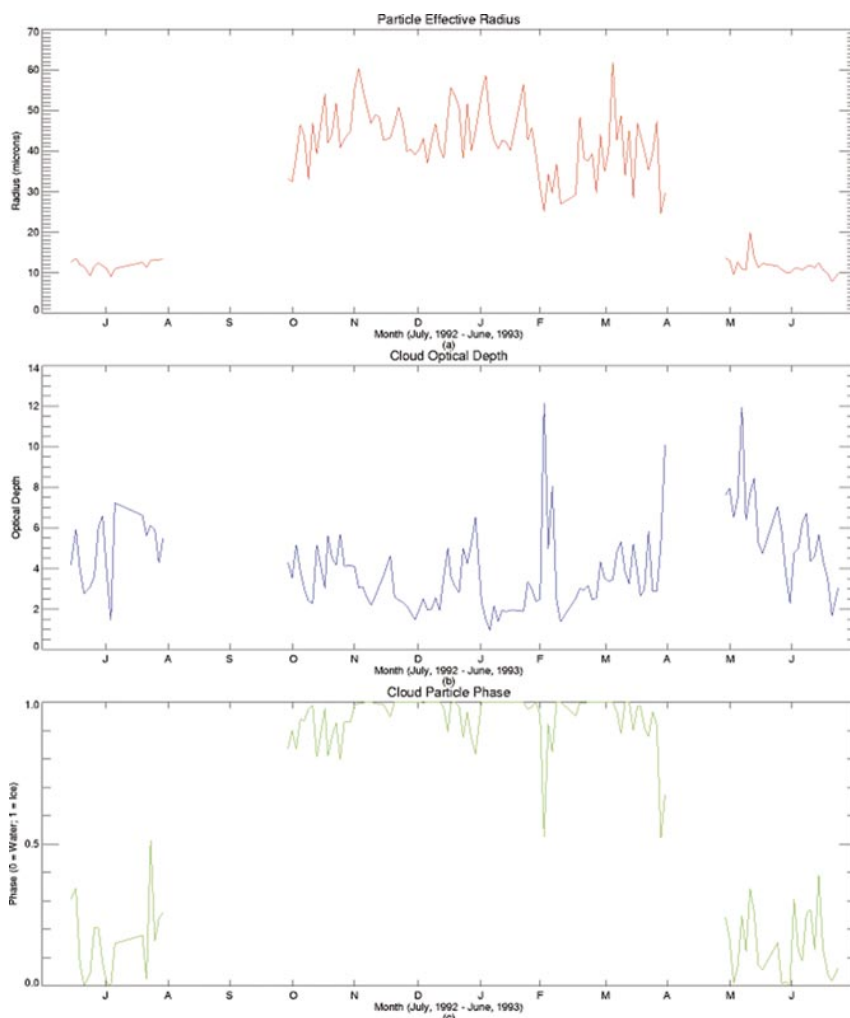


Figure 13. Time series of cloud particle properties: (a) particle effective radius, (b) cloud optical depth, and (c) cloud particle phase.

cloud properties are consistent with the ranges of values expected in the Arctic (Figure 13 and Figure 14), as given by the climatology and model-derived properties described by Curry and Ebert (Curry and Ebert, 1992). The cloud particle effective radius calculations have an estimated uncertainty of 2 μm for water radii and 10 μm for ice radii (Key et al., 1996). The AVHRR-derived values of effective radius agree well with the observations cited by Curry and Ebert. Those observations suggest values are on the order of 5–20 μm for summertime Arctic clouds, with 4.7 μm for midlevel water clouds, 7.5 μm for low-level water clouds, and 40 μm for ice crystal clouds used in the Curry and Ebert (Curry and Ebert, 1992) radiative transfer modeling. The AVHRR-derived effective radii (Figure 13a), though showing considerable variability, are on the order of 40 μm during winter when ice-phase particles dominate. Summer effective radii from AVHRR

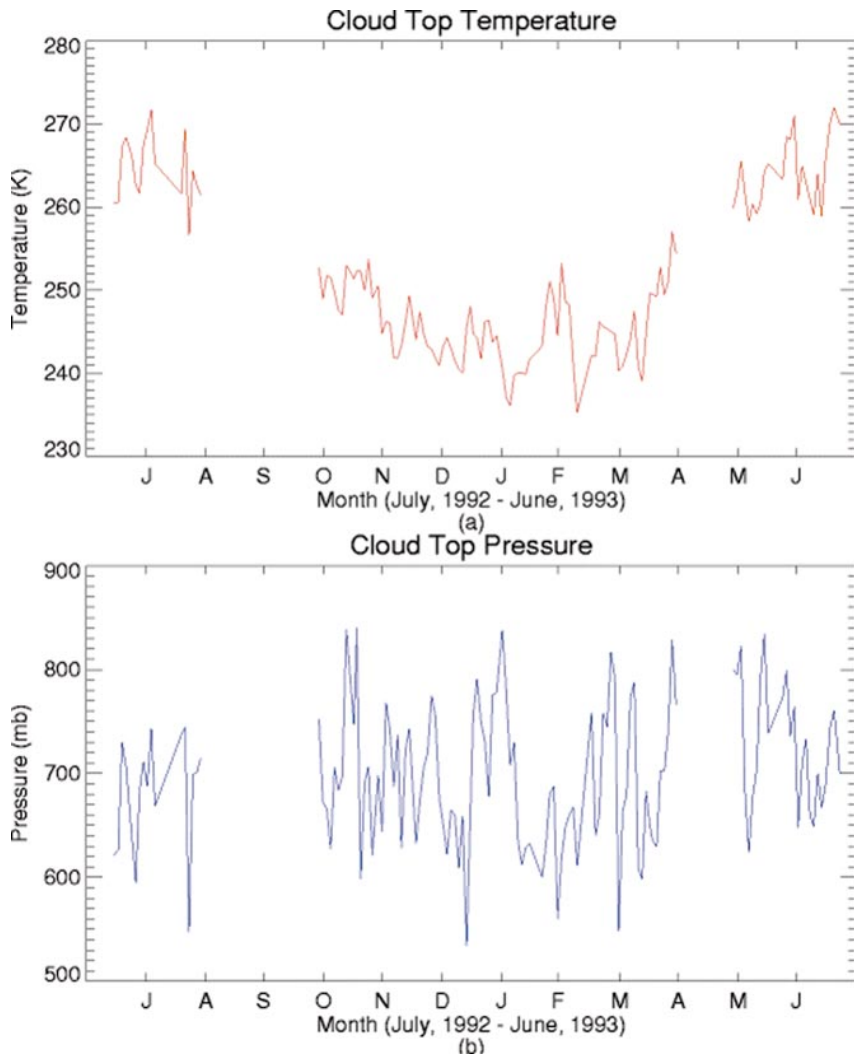


Figure 14. Time series of cloud-top properties: (a) cloud-top temperature and (b) cloud-top pressure.

are about $10 \mu\text{m}$, compared to observations of 10.4 and $13.5 \mu\text{m}$ cited for the Beaufort Sea and Barrow, Alaska (Curry and Ebert, 1992; Table 1).

Calculations of AVHRR-derived cloud optical depth are expected to be less accurate, with potential errors of 50% (Key et al., 1996). This large error is due to uncertainty in calibrations, the small signal-to-noise ratio in AVHRR channel 3 at low temperatures, and uncertainties of cloud phase. Nonetheless, the AVHRR data yield reasonable results in comparison to Curry and Ebert (Curry and Ebert, 1992). Curry and Ebert cite an optical depth of 2–24 for summer water clouds and select values between 6 and 8 for radiative transfer modeling, with an optical depth of approximately 2 for winter conditions. The magnitude of optical depths retrieved from the AVHRR data (Figure 13b) agrees with these estimates. The

AVHRR data, though, show an increase in optical depths to summertime values in April, whereas Curry and Ebert prescribe wintertime conditions through mid-May.

Cloud particle phase estimated from AVHRR (Figure 13c) is also realistic, with ice-phase clouds dominating from October through March, a transition period in April, and liquid-phase clouds in May–July. The timing of the changes in phase is consistent with the observed and AVHRR-derived surface temperatures. Assuming that most of the cloud is low-level cloud occurring near the inversion level, then the change in cloud phase that appears in April is consistent with the surface temperatures plotted in Figure 7, suggesting that the prescription of ice phase through most of April noted above in Curry and Ebert (Curry and Ebert, 1992) may underestimate the presence of water (or possibly mixed phase) clouds. The AVHRR-derived cloud-top temperatures (Figure 14a) correspond with this. AVHRR-derived cloud-top pressures (Figure 14b) are quite variable but suggest higher-level clouds in winter compared to summer, in keeping with observations (Schweiger and Key, 1992). The uncertainty in cloud-top height is estimated to be 50 mb in summer water clouds and 150 mb in winter ice clouds (Key et al., 1996).

As noted earlier, ice transport is a key element controlling the evolution of the sea ice cover. Thus, it is useful to have ice motion information available in conjunction with the energy-budget-related products described above. Under clear skies or optically thin cloud, the AVHRR data provide detailed ice motions and ice edge information. AVHRR also provides useful long-term ice motion calculations, particularly as a complement to other sources of ice motion and when combined with ice velocities from drifting buoys and microwave data (Fowler et al., 1994; Maslanik et al., 1997).

The accuracy and velocity resolution of AVHRR-derived ice motion are related to the spatial resolution of the AVHRR imagery. With the subpixel image registration accuracy of the AVHRR images used here, a minimum error of ± 0.5 pixels is attainable. In comparison with drifting buoys over the 1-yr study period, the mean difference was 0.006 cm s^{-1} with a standard deviation error of $\pm 1.2 \text{ cm s}^{-1}$ (e.g., Emery et al., 1995). Seasonal means of the AVHRR-derived ice motions are consistent with the buoy drift means but also reveal spatial detail not obtainable using the network of drifting buoys. In particular, the motion fields show rapid and localized variability in ice motion and provide ice motion information for areas such as the coastal zones where buoys are typically not deployed.

5. Applications examples

The collocated and coincident product set summarized above is particularly applicable for investigations of regional- and local-scale climate processes. To illustrate how these AVHRR products can be used together and in conjunction with other datasets, we provide some brief application examples below.

5.1. Combining AVHRR products to investigate temperature-albedo relationships and surface heat fluxes

In climate models, complex relationships are often represented using very simple approximations, where one parameter is estimated based on an assumed relation-

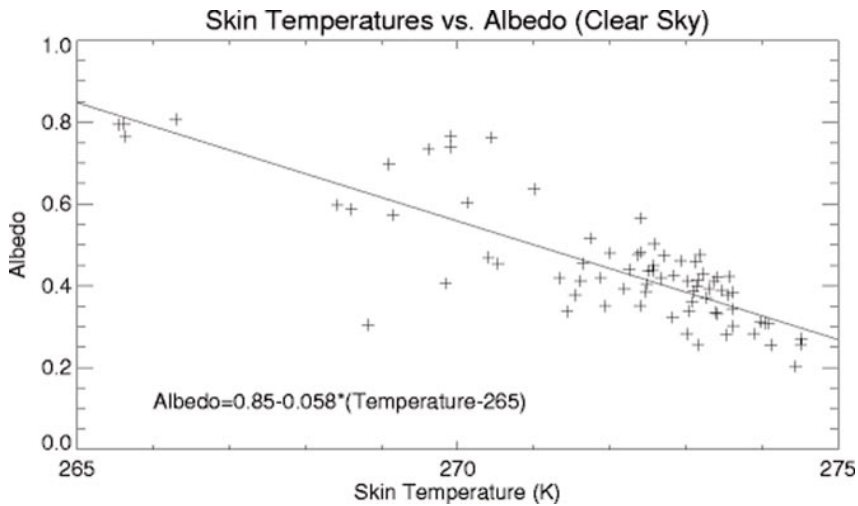


Figure 15. Skin temperature vs surface albedo for clear-sky conditions and areas of at least 50% ice cover. The solid line is the linear best-fit curve.

ship to another parameter. Multivariable datasets such as the AVHRR products provide a means of testing or defining these relationships, or parameterizations, more accurately. One such example is the estimation of surface albedo over sea ice and snow. In this case, the processes controlling albedo are not completely understood, but albedo is known to be correlated to surface temperature. In most climate models, sea ice albedo is prescribed as one value when surface temperatures are below freezing and as a second value once the surface reaches the melting point. The precise albedos used, and the actual relationship between temperature and albedo, are uncertain and based on quite limited studies of sea ice conditions.

Using the collocated AVHRR albedos and skin temperatures for the Beaufort Sea, the temperature–albedo relationship can be investigated in detail. Figure 15, for example, summarizes albedo as a function of skin temperature. In this case, sea ice concentrations derived from Special Sensor Microwave/Imager (SSM/I) passive microwave data (NSIDC, 1996) were coregistered to the AVHRR data and used to identify grid cells with at least 50% ice concentration. For these areas, mean albedo in spring is about 0.85 until skin temperatures reach about 265 K, at which point albedo decreases linearly by 0.058 per degree. The collocated datasets allow such comparisons for large regions and a range of conditions not represented by point measurements. In this case, the degree to which the AVHRR-derived relationship is related to physical processes not represented in simple model parameterizations or to data-related issues remains to be determined. This combination of collocated albedo and skin temperature data can be applied to other regions and conditions to test the accuracy of existing climate model parameterizations and to provide the basis for new parameterizations. For example, meltponds exert significant control over sea ice albedo during summer, but they are not treated explicitly in existing parameterizations used in climate

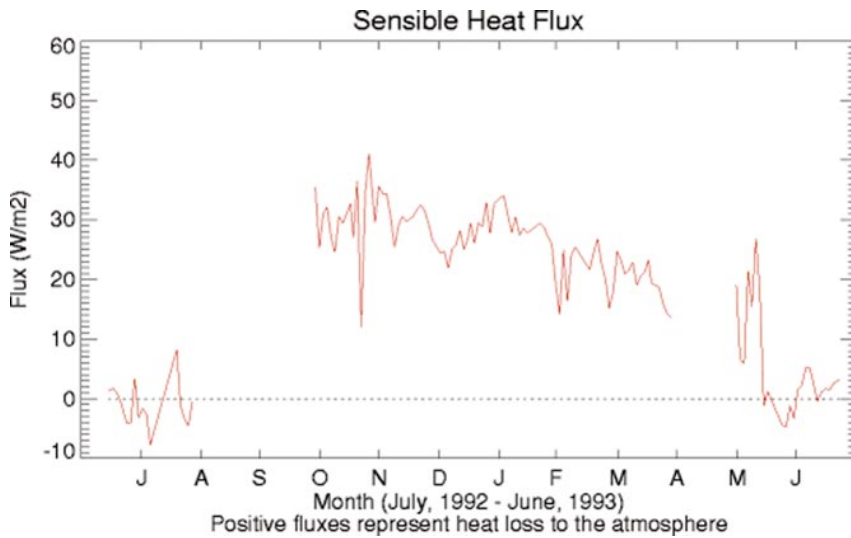


Figure 16. Time series of sensible heat flux.

models. Monitoring the change in areally averaged albedo as a function of melting degree-days and meltpond development, as is planned as part of the SHEBA experiment, should help improve albedo parameterizations.

A key component of climate and process models is the estimation of heat and momentum fluxes using model-predicted variables such as temperature, surface conditions, and wind speed. Uncertainties in each component of the flux calculation introduce errors in the estimated fluxes and in the other modeled conditions that are a function of these parameters. Satellite observations combined with meteorological data can be used to validate the model estimates. Data assimilation techniques go one step further by using observations directly within the model to constrain the predicted fluxes to yield more accurate estimates of desired fields such as ice thickness distributions.

To demonstrate the potential use of the AVHRR products for such applications, sensible heat fluxes were calculated from the Beaufort Sea dataset using a simplified version of the strategy of Lindsay and Rothrock (Lindsay and Rothrock, 1994a). The AVHRR skin temperature was adjusted to represent air temperatures; a fixed wind speed of 5 m s^{-1} was assumed; and fluxes were estimated separately for open water (at 271.2 K) and ice fractional coverage as determined by the SSM/I data noted above. Since turbulent fluxes as calculated here are a linear function of wind speed, use of a fixed wind speed provides only an approximate estimate of actual fluxes.

The flux values range from small negative values in the summer when the warmer atmosphere is adding heat to the ice surface to positive values of $30\text{--}40 \text{ W m}^{-2}$ in the winter where heat is lost from the ocean to the atmosphere, primarily through leads. The relatively large mean fluxes, especially in April and May (Table 2 and Figure 16) likely reflect the inclusion of thin ice in the open-water fraction estimated by SSM/I as well as the marginal ice zone character of some

of the study area, as opposed to ice conditions typical of the central Arctic domain used by Maykut (Maykut, 1978). As more data become available, this approach of estimating turbulent fluxes using combinations of remotely sensed data can be used to assess the accuracy of fluxes estimated by sea ice process models and should help define the relative importance of variables such as open-water fraction and water–ice temperature contrasts in determining accurate surface fluxes.

5.2. Combining datasets to investigate sea ice dynamical processes

Satellite-derived products are well suited for investigating conditions that change rapidly over time and space. One such example is the variability in sea ice concentration as a function of ice transport. The AVHRR-derived datasets, in combination with SSM/I-derived ice concentrations, can be used for individual case studies, particularly when clear-sky areas are large enough to permit AVHRR surface measurements over large areas.

As an example, Figures 17 and Figure 18 show the change in SSM/I-derived ice concentrations over a 3-day period in conjunction with ice drift patterns estimated from AVHRR. In this case, the combination of remotely sensed ice motion and ice concentrations show a strong convergence event along the Canadian coast due to northerly winds arising from a low pressure system in the western Beaufort Sea. Sea ice is advected toward the coast on 18–19 November (Figure 17), causing an increase in ice concentration (decrease in open-water fraction). By 20 November (Figure 18), the coastal zone appears to be filled with ice, such that the continued southward ice drift into the Mackenzie River delta is deflected eastward and westward.

Given that such convergence of the ice pack is a threat to navigation and coastal operations, analyses of these events is of particular interest. In this example, the sea level pressure fields simulated by the NCEP forecast model place the low pressure system farther northward than is suggested by the ice motion patterns, such that winds are easterly along the coast rather than northerly. Thus, ice advection simulated using the NCEP winds would fail to reproduce the observed ice convergence. The types of data discussed here are valuable for identifying the mechanisms involved in such events and in turn help to improve regional ice forecast models.

6. Conclusions

This work describes the assembly, processing, and sample applications of a set of climate parameters estimated from a yearlong AVHRR dataset of the Beaufort Sea. The remotely sensed surface and cloud physical parameters show reasonable agreement with model output, climatologies, and observations. The results indicate that AVHRR-derived parameters show promise for eliciting important physical properties of the polar climate. In particular, AVHRR has the capability to retrieve an internally consistent set of surface and cloud parameters at coincident spatial and temporal resolution. The record of AVHRR imagery acquired since the early 1980s thus has the potential to provide a valuable time series of geo-

INTERACTIONS OF ICE MOTION AND ICE CONCENTRATION

Ice Motion from AVHRR Imagery and Change
in Ice Concentration Over a 24 hr Period

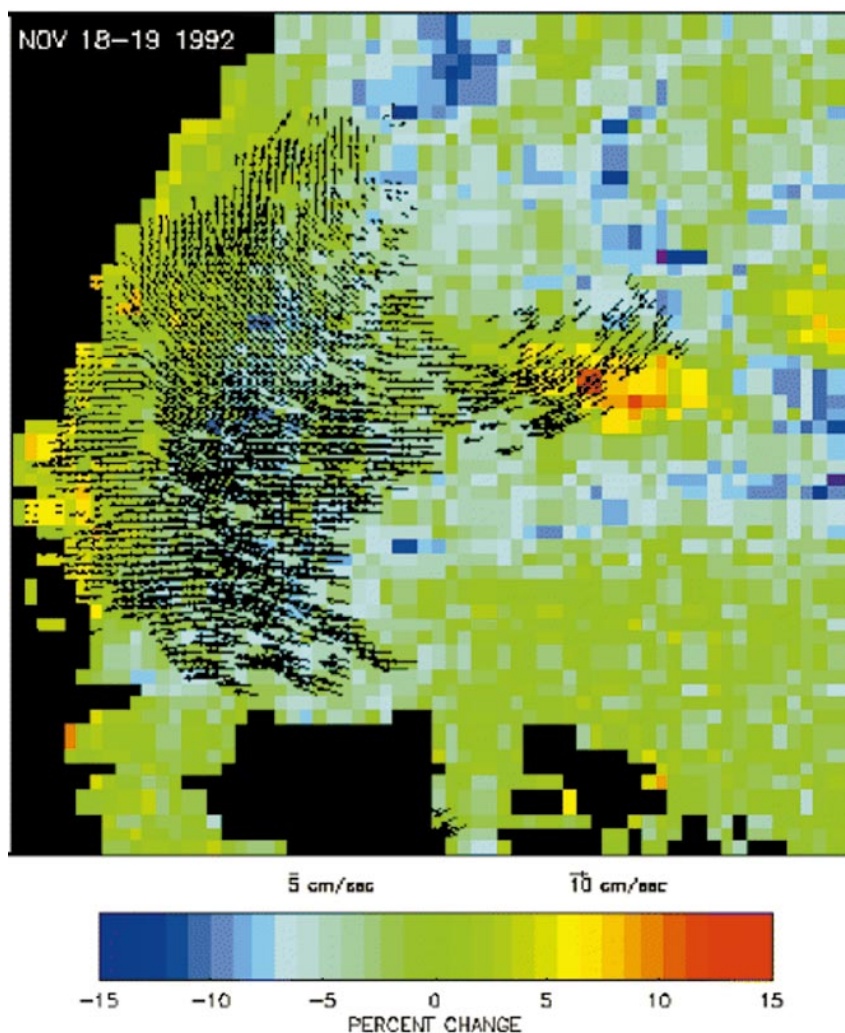


Figure 17. Convergence of the sea ice pack along the Canadian coast, as depicted using a combination of AVHRR-derived ice motions (arrows) and change in first-year ice concentration for 18-19 November.

physical parameters for climate studies. The comparison results also point out the need for more validation and, in particular, the need for well-documented validation datasets that provide extended temporal and/or spatial coverage. Substantial uncertainty thus still remains regarding the accuracy of the individual products, but the data have clear value for analyzing spatial patterns of variability and

INTERACTIONS OF ICE MOTION AND ICE CONCENTRATION

Ice Motion from AVHRR Imagery and Change
in Ice Concentration Over a 24 hr Period

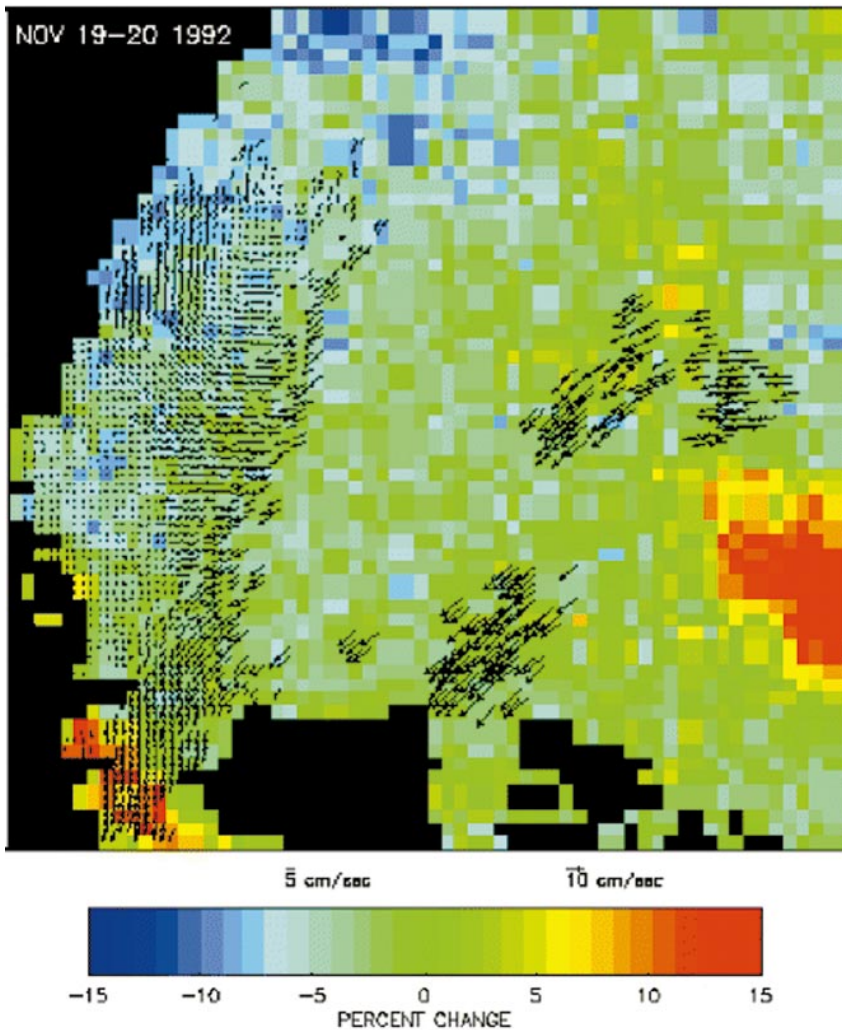


Figure 18. Convergence of the sea ice pack for 19-20 November.

general temporal and spatial relationships among different data types. As noted by a number of investigators (e.g., McGuffie et al., 1988; Kukla and Robinson, 1988; Lindsay and Rothrock, 1994a), cloud screening is a critical and difficult process in estimating clear-sky conditions for polar regions. The most important step to improving the products discussed here pertain to more accurate detection of clouds. Possibilities being investigated include use of temporal and spatial

filters, as well as incorporation of additional remotely sensed data such as TIROS Operational Vertical Sounder and passive microwave imagery.

AVHRR is one among several current and planned sensors employed to gather data in the Arctic. Two other important sensors are the passive microwave Special Sensor Microwave/Imager and the active microwave synthetic aperture radar. Though these have some advantages over AVHRR and many of their capabilities are complementary to AVHRR, AVHRR does have some advantages. For example, while SSM/I can provide daily surface data in both clear and cloudy skies during daylight and darkness, AVHRR provides much finer resolution (12.5–25 km for SSM/I compared to 1.2–5 km for AVHRR). SAR can provide extremely high resolution (30–240 m) imagery during all sky conditions, but operational constraints and orbit configuration limit acquisition of complete Arctic coverage to approximately once per 6 days. The large volume of data generated by SAR also requires considerable postprocessing to provide manageable datasets for large-scale studies. Thus, while when considered separately, each remotely sensed data type available for polar applications has particular limitations, possibilities exist for combining various data types to overcome these limitations. For example, a major limitation of the AVHRR surface products such as albedo and temperature is their restriction to clear-sky conditions. Model applications in particular benefit from the availability of all-sky retrievals. Work is under way to explore methods of combining microwave data and visible- and thermal-band imagery with radiative transfer modeling and data assimilation to generate all-sky surface temperatures.

The example applications suggest several approaches for combining the different geophysical products to investigate polar processes. In particular, the availability of a consistent set of parameters addressing the energy budget and ice transport will assist diagnostic studies of the mechanisms controlling the variability of the sea ice cover, either as part of observations analyses or through improved representation of physical processes in climate models.

Finally, we note that the techniques outlined in this paper, along with algorithm improvements and additional validation, are being used to produce a multiyear time series of polar AVHRR products as part of the NASA Pathfinder effort. These datasets, based on the preliminary work here, will encompass all Arctic and Antarctic regions and are being derived from 4-km-resolution global area coverage data. The derived parameters will be produced for 12 years of data, making long-term studies of the polar regions from AVHRR data feasible. A similar set of higher-resolution (1.25 km) products is also being prepared. Samples of the AVHRR Polar Pathfinder data and the data used here are available via ftp from <http://polarbear.colorado.edu> or via e-mail request to the authors. The Web site also provides processing descriptions as well as plotting and animation capabilities for ice motion data (and soon for browse images of temperature and albedo) being prepared as part of the AVHRR Polar Pathfinder. Links are also available to other groups involved in the integrated Polar Pathfinder effort.

Acknowledgments. Thanks are due to Atmospheric Environment Service, NSIDC, and NOAA for data. This work is funded by NASA's Mission to Planet Earth and the EOS POLES project.

References

- Baldwin, D. and W. J. Emery. 1995. Spacecraft attitude variations of NOAA-11 inferred from AVHRR imagery. *Int. J. Remote Sens*, **16**, 531–548.
- Banks, H. C. and E. N. Partanen. 1959. Meteorological observations. *Scientific Studies at Fletcher's Island, T-3, 1952–1955, AFCRC-TR-59-232(2)*, Vol. II, Air Force Cambridge Res. Lab. Cambridge, MA. 1–49 [Available from Terrestrial Sciences Laboratory, Geophysical Research Directorate, Air Force Cambridge Research Center, U.S. Air Force, Bedford, MA 01730.].
- Barry, R. G., M. C. Serreze, J. A. Maslanik, and R. H. Preller. 1993. The Arctic sea ice-climate system: Observations and modeling. *Rev. Geophys*, **31**, 397–422.
- Burns, B. A., M. Schmidt-Grottrup, and T. Viehoff. 1992. Methods for digital analysis of AVHRR sea ice images. *IEEE Trans. Geosci. Remote Sens*, **30**, 589–602.
- Comiso, J. C. 1994. Surface temperatures in the polar regions from *Nimbus-7* temperature humidity infrared radiometer. *J. Geophys. Res*, **99**, 5181–5200.
- Curry, J. and E. Ebert. 1992. Annual cycle of radiation fluxes over the Arctic Ocean: Sensitivity to cloud optical properties. *J. Clim*, **5**, 1267–1280.
- de Abreu, R. A., J. Key, J. A. Maslanik, M. C. Serreze, and E. F. LeDrew. 1994. Comparison of in situ and AVHRR-derived surface broadband albedo over Arctic sea ice. *Arctic*, **47**, 288–297.
- Dutton, E. G. 1993. An extended comparison between LOWTRAN7 computed and observed broadband thermal irradiances: Global extreme and intermediate surface conditions. *J. Atmos. Oceanic Technol*, **10**, 326–336.
- Ebert, E. and J. Curry. 1992. A parameterization of ice cloud optical properties for climate models. *J. Geophys. Res*, **97**, 3831–3836.
- Ebert, E. and J. Curry. 1993. An intermediate one-dimensional thermodynamic sea ice model for investigating ice–atmosphere interactions. *J. Geophys. Res*, **98**, 10–109.
- Emery, W. J., C. Fowler, J. Hawkins, and R. H. Preller. 1991. Satellite image inferred sea ice motion in Fram Strait, the Greenland Sea and the Barents Sea. *J. Geophys. Res*, **96**, 4751–4768.
- Emery, W. J., C. Fowler, and J. Maslanik. 1994. Arctic sea ice concentrations from special sensor microwave imager and advanced very high resolution radiometer satellite data. *J. Geophys. Res*, **99**, 18–342.
- Emery, W. J., C. Fowler, and J. Maslanik. 1995. Satellite remote sensing of ice motion. *Oceanographic Applications of Remote Sensing*, M. Ikeda and F.W. Dobson. CRC Press. Boca Raton, FL, 367–379.
- Fowler, C., J. A. Maslanik, and W. J. Emery. 1994. Observed and simulated ice motion for an annual cycle in the Beaufort Sea, IGARSS '94, Pasadena, CA. *Proc. IGARSS '94, Pasadena, CA*. NASA, 1303–1305.
- Hu, Y. X. and K. Stamnes. 1993. An accurate parameterization of the radiative properties of water clouds suitable for use in climate models. *J. Clim*, **6**, 728–742.
- Kalnay, E. and Coauthors. 1996. The NCEP/NCAR 40-year reanalysis project. *Bull. Amer. Meteor. Soc*, **77**, 437–471.
- Key, J. 1996a. Streamer user's guide. *Department of Geography Tech. Rep. 96-01*, Boston University. Boston, MA, 72–471 [Available from Jeff Key, Dept. of Geography, Boston University, 675 Commonwealth Ave., Boston, MA 02215.].
- Key, J. 1996b. The Cloud, and Surface Parameter Retrieval (CASPR) System user's guide. *Department of Geography Tech. Rep. 96-02*, Boston University, Boston, MA, 90–471 [Available from Jeff Key, Dept. of Geography, Boston University, 675 Commonwealth Ave., Boston, MA 02215.].

- Key, J. and R. G. Barry. 1989. Cloud cover analysis with Arctic AVHRR. Part 1: cloud detection. *J. Geophys. Res.*, **94**, 18–535.
- Key, J. and M. Haefliger. 1992. Arctic ice surface temperature retrieval from AVHRR thermal channels. *J. Geophys. Res.*, **97**, 5885–5893.
- Key, J., R. Stone, J. Maslanik, and E. Ellefsen. 1993. The detectability of sea ice leads in thermal satellite data as a function of atmospheric conditions and measurement scale. *Ann. Glaciol.*, **17**, 227–232.
- Key, J., J. A. Maslanik, T. Papakyriakou, M. C. Serreze, and A. J. Schweiger. 1994a. On the validation of satellite-derived sea ice surface temperature. *Arctic*, **47**, 280–287.
- Key, J., R. Stone, and M. Rehder. 1994b. Estimating high latitude radiative fluxes from satellite data: problems and successes. *Proc. IGARSS '94*, Vol. 2, Pasadena, CA, NASA, 1018–1020.
- Key, J., R. Stone, and A. Schweiger. 1996. Expected errors in satellite-derived estimates of the high latitude surface radiation budget. *Proc. IGARSS '96*, Lincoln, NE, NASA, 636–638.
- Key, J., J. Collins, C. Fowler, and R. Stone. 1997. High-latitude surface temperature estimates from thermal satellite data. *Remote Sens. Environ.*, **61**, 302–309.
- Koepke, P. 1989. Removal of atmospheric effects from AVHRR albedos. *J. Appl. Meteorol.*, **28**, 1341–1348.
- Kukla, G. J. and D. A. Robinson. 1988. Variability of summer cloudiness in the Arctic Basin. *Meteorol. Atmos. Phys.*, **39**, 42–50.
- Kwok, R., J. Culander, R. McConnell, and S. Pang. 1990. An ice-motion tracking system at the Alaska SAR facility. *IEEE J. Oceanic Eng.*, **15**, 44–54.
- Lindsay, R. W. and D. A. Rothrock. 1994a. Arctic sea ice surface temperature from AVHRR. *J. Clim.*, **7**, 174–183.
- Lindsay, R. W. and D. A. Rothrock. 1994b. Arctic sea ice albedo from AVHRR. *J. Clim.*, **7**, 1737–1749.
- Maslanik, J., C. Fowler, J. Key, T. Scambos, T. Hutchinson, and W. Emery. 1997. AVHRR-based Polar Pathfinder products for modeling applications. *Ann. Glaciol.*, in press..
- Maykut, G. 1978. Energy exchange over young sea ice in the central Arctic. *J. Geophys. Res.*, **83**, 3646–3658.
- McGuffie, K., R. G. Barry, A. Schweiger, D. A. Robinson, and J. Newell. 1988. Intercomparison of satellite-derived cloud analyses for the Arctic Ocean in spring and summer. *Int. J. Remote Sens.*, **9**, 447–467.
- Ninnis, R. M., W. J. Emery, and M. J. Collins. 1986. Automated extraction of pack ice motion from Advanced Very High Resolution Radiometer imagery. *J. Geophys. Res.*, **91**, 10–734.
- NSIDC. 1996. DMSP SSM/I brightness temperatures and sea ice concentration grids for the polar regions. User's guide. 2d ed. National Snow and Ice Data Center, CIRES, Boulder, CO, 110–734.
- Robinson, D. A., M. C. Serreze, R. G. Barry, G. Scharfen, and G. Kukla. 1992. Large-scale patterns and variability of snowmelt and parameterized surface albedo in the Arctic Basin. *J. Clim.*, **5**, 1109–1119.
- Rosborough, G. W., D. G. Baldwin, and W. J. Emery. 1995. Precise AVHRR navigation. *Trans. Geosci. Remote Sens.*, **32**, 644–657.
- Rossow, W. B., R. A. Schiffer. 1991. ISCCP cloud data products. *Bull. Am. Meteorol. Soc.*, **72**, 2–30.
- Schweiger, A. J. and J. R. Key. 1992. Arctic cloudiness: Comparison of ISCCP-C2 and *Nimbus-7* satellite-derived cloud products with a surface-based cloud climatology. *J. Clim.*, **5**, 1514–1527.
- Serreze, M. C. and M. C. Rehder. 1990. June cloud cover over the Arctic Ocean. *Geophys. Res. Lett.*, **17**, 2397–2400.
- Stone, R., T. Mefford, E. Dutton, D. Longenecker, B. Halter, and D. Endres. 1996. Barrow surface

radiation balance measurements, January 1992 to December 1994. *NOAA Data Rep. ERL CMDL-11*, U.S. Department of Commerce, Washington, DC, 81–2400.

Taylor, V. R. and L. L. Stowe. 1984. Atlas of reflectance patterns for uniform earth and cloud surfaces (NIMBUS-7 ERB-61 days). *NOAA Tech. Rep. NESDIS 10*, U.S. Department of Commerce, Washington, DC, 66–2400.

Walter, B. A., J. E. Overland, and P. Turet. 1995. A comparison of satellite-derived and aircraft-measured regional surface sensible heat flux over the Beaufort Sea. *J. Geophys. Res.*, **100**, 4585–4591.

Table 1. AVHRR-derived parameters and comparison with model and observed values. (Comparison values estimated from figures in CE (Curry and Ebert, 1992) and BP (Banks and Partanen, 1959).) NCEP reanalysis values are monthly means averaged over the same area and time period as the AVHRR values (Kalnay et al., 1996).

	Surface temperature (K)				Cloud cover (%)			
	AVHRR	CE	BP	NCEP	AVHRR	CE	ISCCP	NCEP
Jan	233	240	238	244	73	81	50	44
Feb	242	240	235	247	77	78	60	41
Mar	243	242	233	249	56	81	50	41
Apr	254	250	247	256	45	71	41	33
May	269	263	264	267	67	78	30	43
Jun	273	272	271	274	59	83	30	41
Jul	272	273	273	275	50	85	39	44
Aug	272	272	269	274	74	81	43	43
Sep	-	265	262	266	-	85	45	50
Oct	249	254	248	257	74	89	50	46
Nov	241	246	244	248	77	78	48	44
Dec	236	243	241	243	72	78	55	45

Table 2. AVHRR-derived parameters and comparison with model and observed values estimated from figures in CE (Curry and Ebert, 1992), Maykut (Maykut 1978), LR (Lindsay and Rothrock, 1994a), and R et al. (Robinson et al., 1992). For the sensible heat flux results, positive fluxes represent heat loss to the atmosphere.

	Albedo				Sensible heat flux ($W\ m^{-2}$)		
	AVHRR	CE	R et al.	LR	AVHRR	Maykut	LR
Jan	-	0.83	-	-	30	17	10
Feb	-	0.83	-	-	24	16	27
Mar	0.70	0.82	-	0.72	22	12	21
Apr	0.75	0.81	-	0.76	30	9	12
May	0.70	0.80	0.76	-	18	-2	-
Jun	0.51	0.80	0.64	0.56	1	-8	15
Jul	0.43	0.45	0.49	0.49	-2	-	15
Aug	0.44	0.46	0.48	0.47	7	-	-
Sep	-	0.75	-	-	-	-5	20
Oct	-	0.78	-	-	30	-1	23
Nov	-	0.80	-	-	31	6	33
Dec	-	0.82	-	-	27	11	23

Earth Interactions is published jointly by the American Meteorological Society, the American Geophysical Union, and the Association of American Geographers. Permission to use figures, tables, and *brief* excerpts from this journal in scientific and education works is hereby granted provided that the source is acknowledged. Any use of material in this journal that is determined to be “fair use” under Section 107 or that satisfies the conditions specified in Section 108 of the U.S. Copyright Law (17 USC, as revised by PL. 94-553) does not require the publishers’ permission. For permission for any other form of copying, contact one of the copublishing societies.